The Influence of Vortex Sheet Geometry on the Kelvin-Helmholtz Instability*

Ryan Murray & Galen Wilcox†
North Carolina State University, Raleigh, NC, 27606, USA

March 29, 2025

Abstract

This article revisits the instability of sharp shear interfaces, also called vortex sheets, in incompressible fluid flows. We study the Birkhoff-Rott equation, which describes the motion of vortex sheets according to the incompressible Euler equations in two dimensions. The classical Kelvin-Helmholtz instability demonstrates that an infinite, flat vortex sheet has a strong linear instability. We show that this is not the case for circular vortex sheets: such a configuration has a delicate linear stability, and is the first example of a linearly stable solution to the Birkhoff-Rott equation. We subsequently derive a sufficient condition for linear instability of a circular vortex sheet for a family of generalized Birkhoff-Rott kernels, and prove that a common regularized kernel used in numerical simulation and analysis destabilizes the circular vortex sheet. Absent a destabilizing kernel regularization, our work suggests that the nonlinear dynamics are critical for understanding circular vortex sheet instability, and so the essential mechanism of the Kelvin-Helmholtz instability is dependent on global vortex sheet geometry. As expected, nonlinear numerical simulations utilizing the regularized kernel exhibit unstable behavior. Finally, we show experimental results which qualitatively match the types of instabilities that are observed numerically, demonstrating the persistence of the Kelvin-Helmholtz instability in real circular shear flows.

1 Introduction

Sharp shear interfaces are a common feature of a wide variety of real fluid flows. These shear interfaces, which are characterized by a mismatch of tangential velocities along a surface (in three dimensions) or a curve (in two dimensions), appear in wakes, jets, and oceanic as well as atmospheric dynamics. Indeed, one can argue that in many of these applications the most relevant fluid behavior is described by the shear interface.

In the context of inviscid flow, the simplest example of such an interface is the flat vortex sheet in two dimensions, whose velocity is given by

$$u_{KH}(x,t) \equiv u_{KH}(x) = \begin{cases} (u^+, 0) & \text{for } x_2 > 0 \\ (u^-, 0) & \text{for } x_2 < 0 \end{cases}. \tag{1.1}$$

Due to the discontinuity along the surface $x_2 = 0$ this velocity field is not a classical solution of the incompressible Euler equation

$$\partial_t u + u \cdot \nabla u = \nabla p, \qquad \nabla \cdot u = 0. \tag{1.2}$$

*Abbreviated title: Influence of Vortex Sheet Geometry
†Authors ordered alphabetically

However, by rewriting this equation in terms of the vorticity $\omega = \nabla \times u$, we arrive at the system

$$\begin{aligned} &\partial_t \omega + u \cdot \nabla \omega = 0, \\ &u = \int K(x-y)\omega(y)dy, \\ &K(z) := -\frac{1}{2\pi}(-z_2/|z|, z_1/|z|). \end{aligned} \tag{1.3}$$

Equation (1.3) can be interpreted to mean that the vorticity is purely advected by the velocity field in two-dimensions, and that the velocity is determined by a non-local linear operator, namely the Biot-Savart law, acting on the vorticity. This is known as the vorticity-stream formulation of the Euler equation.

The vorticity-stream formulation admits a very weak interpretation in which vorticities are permitted to be measures as opposed to only functions. Such a formulation is both mathematically elegant and applicable to many model flows, such as point vortices, vortex patches, and vortex sheets. In particular, the steady flow u_{KH} corresponds to a flat vortex sheet, where vorticity is a measure supported on the line $x_2 = 0$ and density along the line proportional to $(u^- - u^+)$.

There has been a significant body of work attempting to describe the evolution of shear interfaces in fluids. In particular, if vorticity is supported along a curve $z : [a, b] \times [t_0, t_1] \to \mathbb{C} \sim \mathbb{R}^2$, parametrized by vorticity density, then by manipulating Equation (1.3) one may arrive at the Birkhoff-Rott equation

$$\partial_t z^*(\alpha, t) = \frac{1}{2\pi i} \text{P.V.} \int_a^b \frac{1}{z(\alpha, t) - z(\beta, t)} \, d\beta, \tag{1.4}$$

where P.V. denotes the principal value integral, which is necessitated by the order of the singularity in the integrand as $\beta \to \alpha$. We will let $(\cdot)^*$ denote the complex conjugate throughout the paper. For simplicity in this work we only consider vortex sheet curves under which $z(a, t) = z(b, t)$ for all t when a, b are finite (i.e. a closed curve), or the situation where $[a, b] = \mathbb{R}$. A derivation of this equation from the Euler equation can be found in [46]. A major motivation for studying the Birkhoff-Rott equation is that one can ignore the dynamics away from shear interfaces, which are likely themselves unstable, and instead focus on a simpler curve evolution equation. Indeed the Birkhoff-Rott equation is observed to admit, with varying degrees of rigor, self-similar spiral solutions [9, 10, 14, 13, 19]. However, the Birkhoff-Rott equation is still rather delicate: a more in depth treatment of its analytical properties will be given in Section 1.1.

Perhaps the most striking manifestation of the delicate behavior of this equation can be seen by linearizing its evolution about the flat vortex sheet u_{KH}. We review the classical derivation of the linearized equation and the associated instability in Section 2.1, but the outcome is that the strength of the instability grows linearly with the magnitude of the wavenumber. Instability of the flat sheet is observed both numerically and experimentally, and is known as the Kelvin-Helmholtz instability. In those observations, the flat sheet generally evolves into some number of counter-rotating spiraling interfaces. The term *Kelvin-Helmholtz instability* is used by some authors to refer to the specific linear instability of the flat sheet, and by others to describe the tendency of vortex sheets to break down into spirals; when we refer to the Kelvin-Helmholtz instability we take the more inclusive meaning.

The strength of the linear instability is compelling both in attempting to describe the vortex roll up seen in practice as well as the loss of analyticity of vortex sheets observed in mathematical studies. However, this work seeks to illustrate ways in which linearized analysis of vortex sheet instability may be overly simplistic. We posit that the global geometry of vortex sheets may significantly affect how instabilities are manifest.

In particular, we study the circular vortex sheet of radius R which corresponds to the steady velocity field

$$u_C(x,t) \equiv u_C(x) = \begin{cases} u^+ \frac{x^\perp}{|x|^2} & \text{for } |x| > R \\ u^- \frac{x^\perp}{|x|^2} & \text{for } |x| < R \end{cases}, \tag{1.5}$$

where u^+, u^- are again scalars with $u^+ \neq u^-$. We remark that utilizing the Birkhoff-Rott formulation corresponds to the situation where $u^- = 0$, as otherwise there will be an implicit point vortex at the origin. The circular vortex sheet has physical relevance, including geometric similarity to spiraling fluid phenomena such as ocean eddies and the vortex shedding observed by [36]. Another motivating example of engineering relevance arises from the free boundary layer at the outlet of a nozzle. The boundary layer rolls up downstream via the Kelvin-Helmholtz instability until vorticity is concentrated on an approximately circular band to which inviscid instability theories can be applied [29]. The circular vortex sheet is also similar to the sharp shear layers observed in geophysical flows, including hurricane eyewalls on Earth and storms on the surfaces of gas giants including Saturn [1, 2]. Unlike the latter cases, we study circular vortex sheets at a sufficiently small scale where the rotation of the planet does not provide a stabilizing effect.

It has previously been observed that circular vortex sheets exhibit similar numerical instabilities as the flat vortex sheet [45, 43]. As such, and since a circular sheet locally looks flat, one would anticipate that the linearized analysis of the circular sheet should be similar to that of the flat sheet. Our first main result, stated here informally, establishes that this is not the case.

Theorem 1.1 (Informal)**.** *The linearized evolution of the perturbed circular vortex sheet is stable under the Birkhoff-Rott equation.*

This theorem stands in stark contrast with the flat sheet, and contradicts classical work in the fluid mechanics literature [32, 42]. This discrepancy will be thoroughly explored in Section 2. In any case, our result illustrates the critical influence of vortex sheet geometry on the (in)stability of the Birkhoff-Rott equation. In particular, for the circular sheet it would be crucial to study non-linear effects in order to understand the instabilities: we address this question in a companion work [34]. To our knowledge this is also the first example of a steady solution to the Birkhoff-Rott equation which is not linearly unstable; we give further discussion about this in Section 1.1.

On the other hand, numerical experiments still display unstable effects. Such experiments are necessarily based upon smooth approximations of the Birkhoff-Rott kernel. Our second main contribution derives a matrix representation (when considering sine/cosine modes) of the linearized evolution equation for circular sheets under kernel regularized dynamics, and establishes conditions under which they are stable or unstable. As a particular case, we show that the popular kernel regularization introduced in [21] is linearly unstable for high-frequency perturbations of the circular sheet. Summarized here, this result stands in contrast with the Kelvin-Helmholtz instability on flat sheets, where regularization is known to decrease the instability across high wavenumbers, and highlights the challenge of constructing numerical schemes for the Birkhoff-Rott equation.

Proposition 1.1 (Informal)**.** *High-frequency perturbations of the circular vortex sheet are linearly unstable under the Krasny regularization of the generalized Birkhoff-Rott kernel.*

We now outline the remainder of this work. Section 1.1 provides a more detailed accounting of previous work in this area, including analytical, numerical, and experimental results for vortex sheets. In Section 2 we review the classical linearized analysis for the Kelvin-Helmholtz instability, and then demonstrate how the analysis changes for the circular sheet, culminating

in Theorem 2.2 (a more precise version of Theorem 1.1). In this section we also address the conflict with [32, 42] in detail. In Section 3 we study the problem of linear stability for more general kernels, including those utilized in both numerics and analysis. We derive a characterization of stability, with the condition for linear stability given in Proposition 3.1 and the condition for linear instability given in Proposition 3.2. Next we prove Proposition 3.3, which is a more precise statement of Proposition 1.1 and indicates that the Krasny kernel [21] is unstable under high-frequency perturbations. In Section 4 we review standard numerical methods utilized in studying vortex sheet dynamics and illustrate the instabilities observed numerically, as previously recorded in [45]. Finally, in Section 5 we show experiments demonstrating real instability of the circular vortex sheet. The experimental setup that we use builds upon earlier works studying the stability of storm patterns on Saturn, but our focus is upon how the circular shear layer destabilizes upon removal of stabilizing centrifugal forces. The experiments give an excellent qualitative match of the shapes that we observe numerically, see Figures 7 and 8, which suggests that even though the numerics do not match the analytical linearized stability of the classical Birkhoff-Rott equation, they still may provide predictive utility.

1.1 Related Work

The evolution of vortex sheets has been widely studied in the mathematical literature. The derivations and an in-depth account of many analytical properties of the Birkhoff-Rott equation can be found in the classical book [28], as well as in the introduction of [47].

It is well-known that the Birkhoff-Rott equation is rather delicate, and is ill-posed in the sense of Hadamaard (in appropriate C^k or H^s spaces) [8, 12]. Indeed, one can show that, for closed vortex sheets, if a solution is $C^{1+\rho}$ then it must also be C^∞ [25]. On the positive side, by a Cauchy-Kowalevski type argument, it is known [25] that if a curve is initially analytic then there exists a solution to the Birkhoff-Rott equation for short time. Conditions establishing the equivalence between solutions of Birkhoff-Rott and a weak version of Euler's equation is given in [27]. The connection between solutions of the incompressible Euler equation with vortex sheet initial data and smoothed approximations of the same have also been studied by a number of authors, see e.g. [26, 27].

The Kelvin-Helmholtz instability was first studied in the late 19th century. The modern approach and derivation from the Birkhoff-Rott equation, which has an elegant connection with Fourier analysis and Hilbert transforms, appeared in [12] and is clearly presented in Chapter 9 of [28] as well as Chapter 8 of [42]. Many of the early works about well- and ill-posedness centered on perturbations of the flat sheet. This was partially driven by a number of classic numerical studies which provided evidence for spiral roll up from flat sheets [22, 31]. Experimental observation of the instability and subsequent roll-up of the flat sheet were also well-known at the time, see e.g. the classic book [11]. This type of spiral roll-up is expected to be self-similar, and a wide range of numerical and analytical work has sought to better understand self-similar solutions to Euler's equation which resemble vortex sheets [7, 14, 15, 39, 40, 9, 10].

Numerical methods for vortex sheets require delicate attention, especially in regions where the sheet nearly self-intersects: this can be immediately seen by noticing that the need for a principal value integral in the definition of the Birkhoff-Rott equation. Important classical works regarding numerical approximation of vortex sheets include [23, 35]. Often these methods boil down to discretizing the vortex sheet into point vortices and solving for their evolution with out of the box Runge-Kutta methods. For many classical examples of incompressible vortex sheet evolution, including the Kelvin-Helmholtz instability, it is necessary to replace the singular kernel with a regularized approximation. An excellent overview of this process is presented by [24]. The regularization approach also connects directly with other non-local and kernel-driven evolution equations, such as the α-Euler equations and aggregation equations: these have also

been generalized to vortex sheet evolution and studied analytically and numerically in [3, 45]. These works motivate our study of the generalized Birkhoff-Rott equation in Section 3, and there we give explicit formulas for kernels used in the above sources. We also note that forward in time analytical properties of motion driven by these regularized kernels tend to be much better than those of the standard Birkhoff-Rott equation, see, e.g. [4].

The linearized stability of the circular vortex sheet that we will demonstrate in the present work contradicts a number of older works in the fluid mechanics literature. First, the classical work [29] demonstrates the instability of a circular shear interface with respect to velocity perturbations: that is they study the stability of solutions to Euler's equation perturbing off of the velocity profile given by a circular shear flow. The authors motivate their analysis by considering a fully-developed spiral vortex, and accordingly assume at the top of page 655 that the shape of the discontinuity sheet is constant in time. Since they consider velocity perturbations without allowing changes in geometry, vorticity is induced away from the discontinuity sheet and thus the flow can no longer be modeled as a vortex sheet. We study a rather different situation in the present work because we allow geometric perturbations to the vortex sheet and insist that vorticity remains confined to the perturbed contour. Within this class we obtain a stability result that contrasts with theirs. This aligns with the intuition that the reduction to the Birkhoff-Rott equation should remove certain classes of instabilities.

The second and more delicate conflict is with [32, 42]. These authors worked closely together to develop analysis for an expanding circular vortex sheet under geometric perturbations, from which the instability of a non-expanding sheet can be deduced as a special case. Their argument is based on potential flow theory, but it lacks detail and contains multiple errors. We provide detail about the errors in their analysis in Remark 2.1, but in summary, their analysis assumed that at the linear level Fourier modes were uncoupled, and utilized pressure conditions that neglected linear order terms that would have induced coupling between Fourier modes.

Irrespective of the linear stability analysis, a number of computational studies have demonstrated instability reminiscent of Kelvin-Helmholtz for the circular vortex sheet in regularized simulations of the nonlinear dynamics. Recently [45] numerically studied the (in)stability of circular vortex sheets for a variety of kernels, including the standard Birkhoff-Rott kernel as well as kernels from aggregation equations. In their work they discuss analytical characterization of the linear instability as desirable, but to our knowledge subsequent research in that direction was focused only on the case of gradient type kernels from aggregation equations [20]. Similar numerical experiments were carried out by [43].

Other studies of circular vortex sheets have appeared in the physics and experimental literature. Some of this work is inspired by the observation of a stable hexagonal structure on the north polar surface of Saturn, composed of clouds in relative motion. This structure has persisted without any significant changes since it was first observed by the Voyager spacecraft in 1988 [2, 17]. Since the structure is essentially a perturbed circular shear layer, this physical example is highly relevant to our work.

The hexagon has been studied directly in [1], where the authors postulate that it emerged and persists by the equilibration of vertically uniform jets and shear layers. Such equilibration in the context of Saturn can be attributed to relative rotation of the hexagonal structure with respect to the background rotation of the planet. The study [1] strongly relies upon the earlier work [16], which also experimentally demonstrates the steady equilibriation of polygonal vortex patterns on a shear layer in a rotating fluid.

Outside of the infinite flat and closed circular sheet there are relatively few explicit solutions to the Birkhoff-Rott equation. Two notable examples are limits of the rotating Kirchhkoff ellipse (described, e.g. in [5]) and the Prandtl-Munk vortex [33]. These can be used as building blocks for other families of vortex sheets [37]. The instability of these solutions was recently studied in

[38]: in that case the instability can be rather weak, corresponding to algebraic growth. In their work they study only perturbations of the vortex sheet itself, as opposed to perturbations of the underlying velocity fields as in [29]: we follow the same methodology. Their conclusion is that, for the limit of Kirchhoff ellipses and for the Prandtl-Munk vortices that the instability grows stronger in the wavenumber, and hence is similar in character to the flat sheet Kelvin-Helmholtz instability, a phenomenon that we do not observe in our case.

2 Linearized Analysis of the Birkhoff-Rott Equation

In this section, we conduct a linearized analysis of specific vortex sheet solutions to the classical Birkhoff-Rott equation, namely

$$\partial_t z^*(\alpha,t) = \frac{1}{2\pi i}\text{P.V.}\int \frac{1}{z(\alpha,t)-z(\beta,t)}\,d\beta. \tag{2.1}$$

We begin by reviewing the classical analysis for the flat vortex sheet, and then turn our attention to the circular sheet.

2.1 Kelvin-Helmholtz Instability on Flat Vortex Sheets

In reviewing the linearized theory for the Birkhoff-Rott equation near flat vortex sheets our description will follow the method given in [28]. While this theory is largely classical, it offers an important starting point when we examine the circular vortex sheet in the next subsection. We begin by considering the perturbation of the flat sheet $z : (-\infty,\infty)\times[t_0,t_1] \to \mathbb{C} \sim \mathbb{R}^2$ described by $z(\alpha,t) = \alpha + \xi(\alpha,t)$, where ξ is uniformly smooth and small in $\mathbb{C}$. For $\xi \equiv 0$ we have a constant solution to the classical Birkhoff-Rott Equation (1.4). For a nonzero perturbation we obtain

$$\partial_t z^*(\alpha,t) = \partial_t \xi^*(\alpha,t) = \frac{1}{2\pi i}\text{P.V.}\int_{\mathbb{R}} \frac{1}{\alpha+\xi(\alpha)-\beta-\xi(\beta)}d\beta \tag{2.2}$$

$$= \frac{1}{2\pi i}\text{P.V.}\int_{\mathbb{R}} \frac{1}{\alpha-\beta}\frac{1}{1+\mathcal{E}}d\beta, \tag{2.3}$$

where

$$\mathcal{E} = \frac{\xi(\alpha)-\xi(\beta)}{\alpha-\beta}. \tag{2.4}$$

Because ξ is uniformly small and smooth, so is its spatial derivative $\partial_\alpha\xi$. The quantity $\mathcal{E}$ approximates the difference quotient when β approaches α, so it is small as well. Therefore, we linearize about $\mathcal{E} = 0$ to obtain

$$\frac{1}{2\pi i}\text{P.V.}\int_{\mathbb{R}} \left(\frac{1}{\alpha-\beta} - \frac{\xi(\alpha)-\xi(\beta)}{(\alpha-\beta)^2}\right)d\beta. \tag{2.5}$$

Using the fact that

$$\text{P.V.}\int_{\mathbb{R}} \frac{1}{\beta}d\beta = 0 \tag{2.6}$$

and applying integration by parts on the second term, we obtain

$$\partial_t \xi^*(\alpha,t) = \frac{1}{2}\mathcal{H}\partial_\alpha\xi(\alpha,t), \tag{2.7}$$

where $\mathcal{H}$ is the Hilbert transform

$$\mathcal{H}f(x) = \frac{1}{\pi i}\int_{\mathbb{R}} \frac{f(y)}{y-x}dy. \tag{2.8}$$

If we write ξ as the Fourier mode

$$\xi(\alpha,t) = A_k(t)e^{ik\alpha} + A_{-k}(t)e^{-ik\alpha}, k \in \mathbb{Z}, \tag{2.9}$$

then the Hilbert transform of $\partial_\alpha \xi$ is given by

$$\mathcal{H}\partial_\alpha \xi(\alpha,t) = ikA_k(t)e^{ik\alpha} + ikA_{-k}(t)e^{-ik\alpha}. \tag{2.10}$$

For further discussion of the Hilbert transform in the context of this problem, see [28]. This transform is then used to solve the linearized Equation (2.7), yielding expressions for the $\pm k$ Fourier coefficients

$$A_k(t) = A_k^+ e^{kt/2} + A_k^- e^{-kt/2}, \tag{2.11}$$

$$A_{-k}(t) = A_{-k}^+ e^{kt/2} + A_k^- e^{-kt/2}, \tag{2.12}$$

where $A_k^+ = -iA_{-k}^{+*}$ and $A_k^- = iA_{-k}^{-*}$ are determined by the values of $A_{\pm k}$ at time zero. We note coupling between the $\pm k$ Fourier modes. We also see that a component of the k Fourier mode grows exponentially as $e^{|k|t/2}$, implying that the linear evolution problem is highly unstable. Indeed, the instability grows in wavenumber, a fact that some authors describe as a common theme of instability of vortex sheets [38]. The authors of [28] go on to show that there is a family of initially analytic solutions to Equation (2.7) which develop a singularity in finite time.

2.2 Linearized Stability for Circular Vortex Sheets

We now consider the evolution of a circular vortex sheet $z : [0, 2\pi] \times [t_0, t_1] \to \mathbb{C} \sim \mathbb{R}^2$ described by $z(\alpha, t) = e^{i(\alpha + t/2)}$ for $\alpha \in [0, 2\pi]$. As for the planar Kelvin-Helmholtz instability, our starting point is the classical Birkhoff-Rott Equation (3.1). To verify that z is a solution, we compute

$$\partial_t z^*(\alpha,t) = \frac{1}{2\pi i}\text{P.V.}\int_0^{2\pi} \frac{1}{z(\alpha,t) - z(\beta,t)}d\beta \tag{2.13}$$

$$= \frac{e^{-i(\alpha+Ct)}}{2\pi i}\text{P.V.}\int_0^{2\pi} \frac{1}{1-e^{i(\beta-\alpha)}}d\beta. \tag{2.14}$$

In order to simplify our expressions, we will utilize the following generalized formula for the principal value of the Cauchy integral [6, 18], which also holds for points on the boundary of the domain after utilizing principle values: we state it here concretely for convenience of the reader.

Lemma 1 (Cauchy integral formula for Jordan curves)**.** *Let Γ be a rectifiable, closed, positively oriented Jordan curve in $\mathbb{C}$ which defines the interior region Ω^- and exterior region Ω^+. Let $f : \Gamma \to \mathbb{C}$ be an analytic function and $w_0 \in \mathbb{C}/\Gamma$. The well-known Cauchy integral formula states*

$$\frac{1}{2\pi i}P.V.\int_\Gamma \frac{f(w)}{w-w_0}dw = \begin{cases} f(w_0) & \text{for } w_0 \in \Omega^- \\ 0 & \text{for } w_0 \in \Omega^+ \end{cases}. \tag{2.15}$$

Now suppose $w_0 \in \Gamma$; then the Cauchy integral of f at w_0 takes the principal value

$$\frac{1}{2\pi i}P.V.\int_\Gamma \frac{f(w)}{w-w_0}dw = \frac{f(w_0)}{2}. \tag{2.16}$$

Continuing our computation from above, after changing variables to the unit circle (oriented counterclockwise) with the relation $w = e^{i(\beta-\alpha)}$ we obtain by Lemma 1

$$\frac{-e^{-i(\alpha+Ct)}}{2\pi}\text{P.V.}\int_{\partial B}\frac{1}{w(1-w)}dw \tag{2.17}$$

$$= \frac{-e^{-i(\alpha+Ct)}}{2\pi}\text{P.V.}\int_{\partial B}\frac{1}{w}-\frac{1}{w-1}dz \tag{2.18}$$

$$= -i/2e^{-i(\alpha+Ct)}. \tag{2.19}$$

For this initial condition the left-hand side of the Birkhoff-Rott equation is

$$\partial_t z^*(\alpha,t) = -iCe^{-i(\alpha+Ct)}, \tag{2.20}$$

implying that for $C = 1/2$ the circle is a solution to the Birkhoff-Rott equation. This solution z takes the form of a traveling wave corresponding to a steady vorticity distribution; this stands in contrast with the infinite flat sheet studied for the classical Kelvin-Helmholtz instability in which points on the steady sheet do not move.

2.2.1 Additive Perturbations and Fourier Coupling

We will now examine the linear stability of the steady circular sheet by considering a smooth, 2π-periodic perturbation $\xi(\alpha,t)$ where $||\xi||_{C^2} \ll 1$. First, we parallel the classical additive approach to the planar Kelvin-Helmholtz instability by writing $z(\alpha,t) = e^{i(\alpha+t/2)} + \xi(\alpha,t)$, and by representing the perturbation by its Fourier series expansion $\xi(\alpha,t) = \sum A_k(t)e^{i(k\alpha+t/2)}$ with $k \in \mathbb{Z}$. The right-hand side of the Birkhoff-Rott equation becomes

$$\partial_t z^*(\alpha,t) = \frac{1}{2\pi i}\text{P.V.}\int_0^{2\pi}\frac{1}{z(\alpha,t)-z(\beta,t)}d\beta \tag{2.21}$$

$$= \frac{1}{2\pi i}\text{P.V.}\int_0^{2\pi}\frac{1}{e^{i(\alpha+t/2)}-e^{i(\beta+t/2)}+\sum A_k e^{i(k\alpha+t/2)}-\sum A_k e^{i(k\beta+t/2)}}d\beta \tag{2.22}$$

$$= \frac{e^{-it/2}}{2\pi i}\text{P.V.}\int_0^{2\pi}\frac{1}{e^{i\alpha}-e^{i\beta}}\frac{1}{1+\mathcal{E}}d\beta, \tag{2.23}$$

where $\mathcal{E}$ is the small quantity

$$\mathcal{E} = \sum_{k\in\mathbb{Z}} A_k\frac{e^{ik\alpha}-e^{ik\beta}}{e^{i\alpha}-e^{i\beta}}. \tag{2.24}$$

The smallness of $\mathcal{E}$ follows from the assumption that $||\xi||_{C^2} \ll 1$. Taylor expanding about $\mathcal{E} = 0$ to first order, we obtain

$$\partial_t(e^{i(\alpha+t/2)}+\xi(\alpha,t))^* \approx \frac{e^{-it/2}}{2\pi i}\text{P.V.}\int_0^{2\pi}\frac{1}{e^{i\alpha}-e^{i\beta}}-\sum_{k\in\mathbb{Z}}A_k\frac{e^{ik\alpha}-e^{ik\beta}}{(e^{i\alpha}-e^{i\beta})^2}d\beta. \tag{2.25}$$

Noting that the first term in the integral corresponds to the Birkhoff-Rott equation for the steady circular sheet leads to an equation for the perturbation

$$\partial_t(\xi(\alpha,t))^* \approx -\sum_{k\in\mathbb{Z}}A_k\frac{e^{i((k-2)\alpha-t/2)}}{2\pi i}\text{P.V.}\int_0^{2\pi}\frac{1-e^{ik(\beta-\alpha)}}{(1-e^{i(\beta-\alpha)})^2}d\beta. \tag{2.26}$$

Now we change variables to integrate around the unit circle by $w = e^{i(\beta-\alpha)}$, so the right-hand side becomes

$$\sum_{k\in\mathbb{Z}} A_k \frac{e^{i((k-2)\alpha - t/2)}}{2\pi} \text{P.V.} \int_{\partial B} \frac{1-w^k}{w(1-w)^2} dw. \tag{2.27}$$

By using a telescoping sum and partial fraction expansion this may be rewritten as

$$\sum_{k\in\mathbb{Z}} A_k \frac{e^{i((k-2)\alpha - t/2)}}{2\pi} \sum_{j=0}^{k-1} \text{P.V.} \int_{\partial B} \frac{w^j}{w} - \frac{w^j}{w-1} dw, \tag{2.28}$$

and so we can use Lemma 1 to compute

$$\sum_{j=0}^{k-1} \text{P.V.} \int_{\partial B} \frac{w^j}{w} - \frac{w^j}{w-1} dw = \sum_{j=0}^{k-1} (0 - \pi i) = -k\pi i. \tag{2.29}$$

Substituting into (2.26), using an integrating factor to absorb the $e^{-it/2}$ term, and rearranging yields the evolution equation

$$\partial_t \sum_{k\in\mathbb{Z}} A_k^*(t) e^{-ik\alpha} = i/2 \sum_{k\in\mathbb{Z}} \left(A_k^*(t) e^{-ik\alpha} - A_k(t) k e^{i(k-2)\alpha} \right). \tag{2.30}$$

The preceding analysis followed the classical approach to the Kelvin-Helmholtz instability on a flat sheet by using a perturbation form which is added to the steady state. For the flat sheet, the $\pm k$ Fourier modes are coupled. By examining Equation 2.30, we notice an asymmetric coupling between the Fourier modes, specifically that perturbation of the k mode leads to evolution of both the k and $2-k$ modes. Accordingly we can reduce the summation over $k \in \mathbb{Z}$ in Equation (2.30) to a sum of only k and $2-k$ modes. Then by separating the Fourier coefficients A_k into real and imaginary parts as $A_k(t) = B_k(t) + iC_k(t)$, we can write Equation (2.30) in matrix form

$$\frac{d}{dt} \begin{bmatrix} B_k \\ C_k \\ B_{2-k} \\ C_{2-k} \end{bmatrix} = \begin{bmatrix} 0 & 1/2 & 0 & (2-k)/2 \\ -1/2 & 0 & (2-k)/2 & 0 \\ 0 & k/2 & 0 & 1/2 \\ k/2 & 0 & -1/2 & 0 \end{bmatrix} \begin{bmatrix} B_k \\ C_k \\ B_{2-k} \\ C_{2-k} \end{bmatrix}. \tag{2.31}$$

The eigenvalues of this system are $\lambda = \pm i\sqrt{(k-1)^2}$, each with a geometric multiplicity of two. The matrix can be completely diagonalized about these eigenvalues, thereby implying stable oscillation of the perturbation about the circular vortex sheet. Our methods have followed the classical approach to the Kelvin-Helmholtz instability on a flat sheet, but linear stability is obtained instead. This result is striking and further discussion will be provided in the following subsection; there, we will show how an alternative perturbation leads to an elegant closed-form solution to the evolution equation, and formally state our main result.

We also notice that there are some special cases of Equation (2.30). In particular, the $k = 0$ mode depends on $k = 2$ and $k = 0$, but the $k = 2$ mode is independent of the $k = 0$ mode. This first case is because perturbations in the $k = 0$ mode correspond to simple translation of the steady circular sheet. We also observe that the $k = 1$ mode is independent, and in this second case the perturbation remains constant, corresponding to increasing the radius of the steady state. It makes sense that we can uniformly increase the radius of the steady circular sheet and obtain another steady solution.

The linearized stability and Fourier coupling obtained here leads to the following remark, which will resolve the conflict between our main result and the work of [32, 42].

Remark 2.1. *The authors of [32, 42] use potential flow theory to argue that an expanding circular vortex sheet is unstable under geometric perturbations, which is the exactly the opposite of the result we have just established: accordingly we detail their arguments here and explain a flaw in their analysis. While their analysis treats more general settings, namely expanding sheets, we simplify their expressions to match the situation without sheet expansion (which in their notation amounts to* $\dot{R} \equiv 0$*).*

In the present context, the authors of [32, 42] study the undisturbed flow

$$u_r(r,\theta,t) = 0,\ u_\theta(r,\theta,t) = \begin{cases} 0 & \text{for } r < R \\ \frac{\Gamma}{2\pi r} & \text{for } r > R \end{cases}, \tag{2.32}$$

which corresponds to a circular vortex sheet of radius R*, the same circular vortex sheet studied in the present work. The authors represent the perturbed sheet in polar* (r,θ) *coordinates as*

$$r = R + \varepsilon(t)e^{ik\theta}. \tag{2.33}$$

Note that the perturbation is added to the steady state, just as we have done in our preceding analysis.

Next the authors assume an ansatz for the corresponding velocity potentials

$$\phi = \begin{cases} A(t)r^k e^{ik\theta} & \text{for } r < R + \varepsilon(t)e^{ik\theta} \\ \frac{\Gamma\theta}{2\pi} + B(t)r^{-k}e^{ik\theta} & \text{for } r > R + \varepsilon(t)e^{ik\theta} \end{cases}, \tag{2.34}$$

which uses only the k *Fourier mode. We notice that this velocity potential does indeed satisfy the Laplace equation away from the vortex sheet ansatz* (2.33)*, and hence is a valid velocity potential. However, for this to accurately describe the motion of the vortex sheet we need appropriate kinematic and pressure conditions along the sheet itself. These were presented in [32, 42]*[1] *as*

$$\frac{D}{Dt}(R + \varepsilon(t)e^{ik\theta} - r) = 0, \tag{2.35}$$

$$\frac{\partial}{\partial\theta}\left[\frac{\partial\phi}{\partial t} + \frac{1}{2}(|\nabla\phi|)^2\right] = 0. \tag{2.36}$$

Here $[x]$ *indicates the difference in the quantity* x *across the vortex sheet. The first of these conditions is a kinematic condition, amounting to the fact that the sheet is advected by the flow. The second of these conditions is attempting to address the fact that the pressure difference is constant across the sheet (as the value in brackets is equal to the pressure by Bernoulli's equation).*

Substituting Equation (2.34) *into Equations* (2.35) *and* (2.36)*, linearizing, and solving the resulting system of three equations leads to an equation for the amplitude* $\varepsilon(t)$*:*

$$\ddot{\varepsilon} + \dot{\varepsilon}\frac{ik\Gamma}{2\pi R^2} - \varepsilon\frac{k(k-1)\Gamma^2}{8\pi^2 R^4} = 0. \tag{2.37}$$

From Equation (2.37) *the authors deduce that the circular vortex sheet is unstable in the sense that* $|\varepsilon(t)|$ *is unbounded as* $t \to \infty$*. Equation* (2.37) *represents decoupled evolution of the* k *Fourier mode as described by Equation* (2.34)*. This complete Fourier decoupling is not what we observe in our analysis, and furthermore is not observed on the level of the flat vortex sheet.*

[1] We mention that [32] does not provide this level of detail, but does acknowledge the assistance of Saffman, and [42] provides these equations.

The issue with the analysis in [32, 42] arises from the pressure condition (2.36)*. The correct pressure condition, precisely tracking the tangential derivative of the pressure difference along the sheet, should instead read that*

$$\left(\frac{\partial}{\partial\theta} + ik\varepsilon(t)e^{ik\theta}\frac{\partial}{\partial r}\right)\left[\frac{\partial\phi}{\partial t} + \frac{1}{2}(|\nabla\phi|)^2\right] = 0. \tag{2.38}$$

The second term in the derivatives does not disappear upon linearization, and the leading multiplier leads to Fourier coupling. In words, if the sheet has an order ε perturbation of the circle, then the tangential derivatives are not approximated up to order ε by the tangential derivatives for the circle. This error renders their analysis incorrect. In fact, the uncoupled Fourier representation that they utilize is only possible due to their (incorrect) pressure condition.

We mention that the velocity potential approach that those authors follow is precisely how one derives the Birkhoff-Rott equation [28], and had the pressure condition been correctly resolved they would have arrived at the same equations which we derived above. The fact that the Birkhoff-Rott equations already correctly encodes the pressure, kinematic, and potential flow conditions helps our analysis avoid similar pitfalls.

2.2.2 Alternative derivation and transport equation

Our previous analysis has already indicated that a circular vortex sheet is linearly stable. However, the asymmetric Fourier coupling observed in the previous subsection motivates us to explore a slightly different form for the perturbation, which will lead to more transparent analysis and an elegant closed-form solution to the evolution equation. We again consider a smooth, 2π-periodic perturbation $\xi(\alpha,t)$ where $||\xi||_{C^2} \ll 1$. The perturbed circular vortex sheet will now be defined by $z(\alpha,t) = e^{i(\alpha+t/2)}(1+\xi(\alpha,t))$. We then rewrite the right-hand side of the Birkhoff-Rott equation as

$$\partial_t z^*(\alpha,t) = \frac{1}{2\pi i}\text{P.V.}\int_0^{2\pi}\frac{1}{z(\alpha,t)-z(\beta,t)}d\beta \tag{2.39}$$

$$= \frac{e^{-i(\alpha+t/2)}}{2\pi i}\text{P.V.}\int_0^{2\pi}\frac{1}{1+\xi(\alpha)-e^{i(\beta-\alpha)}(1+\xi(\beta))}d\beta \tag{2.40}$$

$$= \frac{e^{-i(\alpha+t/2)}}{2\pi i}\text{P.V.}\int_0^{2\pi}\frac{1}{1-e^{i(\beta-\alpha)}}\frac{1}{1+\mathcal{E}}d\beta, \tag{2.41}$$

where $\mathcal{E}$ is the small quantity

$$\mathcal{E} = \frac{\xi(\alpha)-e^{i(\beta-\alpha)}\xi(\beta)}{1-e^{i(\beta-\alpha)}}. \tag{2.42}$$

As before, the smallness of $\mathcal{E}$ follows from the assumption that $||\xi||_{C^2} \ll 1$. Taylor expanding about $\mathcal{E}=0$ to first order, we obtain

$$\partial_t(e^{i(\alpha+t/2)}(1+\xi(\alpha,t)))^* \approx \frac{e^{-i(\alpha+t/2)}}{2\pi i}\text{P.V.}\int_0^{2\pi}\frac{1}{1-e^{i(\beta-\alpha)}} - \frac{\xi(\alpha)-e^{i(\beta-\alpha)}\xi(\beta)}{(1-e^{i(\beta-\alpha)})^2}d\beta \tag{2.43}$$

which implies that the perturbation ξ evolves by

$$\partial_t(e^{i(\alpha+t/2)}\xi(\alpha,t))^* \approx \frac{-e^{-i(\alpha+t/2)}}{2\pi i}\text{P.V.}\int_0^{2\pi}\frac{\xi(\alpha)-e^{i(\beta-\alpha)}\xi(\beta)}{(1-e^{i(\beta-\alpha)})^2}d\beta. \tag{2.44}$$

We change variables by $w = e^{i(\beta-\alpha)}$, and let $\tilde{\xi}(w) = \xi(\beta)$ so that $\tilde{\xi}(1) = \xi(\alpha)$. The right-hand side then becomes

$$\frac{e^{-i(\alpha+t/2)}}{2\pi}\text{P.V.}\int_{\partial B}\frac{\tilde{\xi}(1)-w\tilde{\xi}(w)}{w(1-w)^2}dw \tag{2.45}$$

$$=\frac{e^{-i(\alpha+t/2)}}{2\pi}\text{P.V.}\int_{\partial B}(\tilde{\xi}(1)-w\tilde{\xi}(w))\left(\frac{1}{w}-\frac{1}{w-1}+\frac{1}{(w-1)^2}\right)dw. \tag{2.46}$$

To apply the Cauchy integral formula, we need $\tilde{\xi}(w)$ to be analytic in w. To this end, we require that $\xi((\ln w)/i+\alpha,t)$ is analytic in w for w in the neighborhood of the unit disc. The Fourier modes e^{ikx} are an example of such a perturbation, and such functions are dense in many relevant function spaces, such as $L^2(\mathbb{S})$. For the first term in (2.46) we may then use the classical Cauchy integral formula (i.e. the first part of Lemma 1) to directly compute

$$\frac{e^{-i(\alpha+t/2)}}{2\pi}\text{P.V.}\int_{\partial B}\frac{\tilde{\xi}(1)-w\tilde{\xi}(w)}{w}dw = ie^{-i(\alpha+t/2)}\tilde{\xi}(1) = ie^{-i(\alpha+t/2)}\xi(\alpha). \tag{2.47}$$

For the second and third terms in (2.46) we Taylor expand the numerator $\tilde{\xi}(1)-w\tilde{\xi}(w)$ about $w=1$ as

$$\tilde{\xi}(1)-w\tilde{\xi}(w) = (-\tilde{\xi}'(1)-\tilde{\xi}(1))(w-1)+R_1(w)(w-1)^2, \tag{2.48}$$

where the remainder $R_1(w)$ is analytic. Substituting this Taylor expansion into the remaining terms of (2.46) yields

$$\frac{e^{-i(\alpha+t/2)}}{2\pi}\text{P.V.}\int_{\partial B}(\tilde{\xi}'(1)+\tilde{\xi}(1))(1-\frac{1}{(w-1)})+R_1(w)(1-(w-1))\,dw. \tag{2.49}$$

The classical Cauchy integral formula cancels the first, third, and fourth of these terms. Utilizing Lemma 1 then returns

$$\frac{e^{-i(\alpha+t/2)}}{2\pi}\text{P.V.}\int_{\partial B}\frac{-\tilde{\xi}'(1)-\tilde{\xi}(1)}{w-1}dw = i/2e^{-i(\alpha+t/2)}(-\tilde{\xi}'(1)-\tilde{\xi}(1)) \tag{2.50}$$

$$= e^{-i(\alpha+t/2)}(-1/2\partial_\alpha\xi(\alpha)-i/2\xi(\alpha)). \tag{2.51}$$

Returning to (2.44), after taking the derivatives of the left -hand side and collecting terms we obtain

$$e^{-i(\alpha+t/2)}(-i/2\xi^*(\alpha,t)+\partial_t\xi^*(\alpha,t)) = e^{-i(\alpha+t/2)}(i\xi(\alpha,t)-i/2\xi(\alpha,t)-1/2\partial_\alpha\xi(\alpha,t)) \tag{2.52}$$

which simplifies to the partial differential equation

$$\partial_t\xi^*(\alpha,t) = i/2(\xi(\alpha,t)+\xi^*(\alpha,t))-1/2\partial_\alpha\xi(\alpha,t) \tag{2.53}$$

or equivalently,

$$\partial_t\xi^*(\alpha,t) = iRe(\xi(\alpha,t))-1/2\partial_\alpha\xi(\alpha,t). \tag{2.54}$$

Although we applied a specific analyticity assumption to ξ so we could manipulate the Cauchy integrals, this linearized equation makes sense for a wide class of perturbations. Indeed, as all of the manipulations were justified for the standard Fourier basis, we can treat this expression as equivalent within the space of L^2 perturbations.

This equation admits a closed form solution by the method of characteristics. Writing the perturbation as a sum of real and imaginary parts $\xi = \xi_R + i\xi_I$, Equation (2.54) becomes

$$\partial_t(\xi_R(\alpha,t)-i\xi_I(\alpha,t)) = i\xi_R(\alpha,t)-\frac{1}{2}\partial_\alpha(\xi_R(\alpha,t)+i\xi_I(\alpha,t)). \tag{2.55}$$

Splitting the previous equation into real and imaginary parts yields

$$\partial_t \xi_R(\alpha,t) + 1/2\partial_\alpha \xi_R(\alpha,t) = 0, \tag{2.56}$$

$$-\partial_t \xi_I(\alpha,t) - \xi_R(\alpha,t) + \frac{1}{2}\partial_\alpha \xi_I(\alpha,t) = 0. \tag{2.57}$$

First consider the real part $\partial_t \xi_R(\alpha,t) + 1/2\partial_\alpha \xi_R(\alpha,t) = 0$. By the method of characteristics we obtain

$$\xi_R(\alpha,t) = f_1(\alpha - t/2), \tag{2.58}$$

where $f_1(\alpha_0)$ is the real initial data as a function of the spatial coordinate. The characteristics for the real part are $t(s) = s$ and $\alpha(s) = s/2 + \alpha_0$. For the imaginary part $-\partial_t \xi_I(\alpha,t) - \xi_R(\alpha,t) + \frac{1}{2}\partial_\alpha \xi_I(\alpha,t) = 0$ we use the method of characteristics to obtain

$$\xi_I(\alpha,t) = f_2(\alpha + t/2) + \int_0^t f_1(\alpha - w/2)dw, \tag{2.59}$$

where $f_2(\alpha_0)$ is the imaginary initial data as a function of the spatial coordinate. The imaginary part has characteristic curves $t(s) = -s$ and $\alpha(s) = s/2 + \alpha_0$. Note that although the characteristic directions in time are different, we can still solve Equation (2.54) because the real part is decoupled. The combination of real and imaginary parts gives the closed-form solution

$$\begin{aligned} \xi_R(\alpha,t) &= f_1(\alpha - t/2), \\ \xi_I(\alpha,t) &= f_2(\alpha + t/2) + \int_0^t f_1(\alpha - w/2)dw, \end{aligned} \tag{2.60}$$

where f_1, f_2 are arbitrary initial data.

We notice that as long as f_1 has mean zero, then both ξ_R, ξ_I remain bounded, in the sense that $\|\xi_R(\cdot,t)\|_2 < C\|\xi(\cdot,0)\|_2, \|\xi_I(\cdot,t)\|_2 < C\|\xi(\cdot,0)\|_2$, with C independent of t and ξ. We also notice that the same bounds are true in L^∞. If f_1 has non-zero mean then we can re-center our solution about another steady state (i.e. a circle with slightly bigger radius).

Hence we have proved the following:

Theorem 2.2. *When linearized about the circular vortex sheet, the Birkhoff-Rott equation can be written as a complex-valued transport equation on the circle, namely Equation* (2.54)*. This equation admits an explicit solution formula* (2.60)*, and assuming the original equation is appropriately centered (i.e. the perturbations have average real part of zero) then this solution map is uniformly stable in both L^2 and L^∞.*

The proof of this theorem follows a similar approach to the Kelvin-Helmholtz instability on a flat sheet, but with a completely different result: that perturbations of the circular sheet are uniformly stable. They are, in essence, governed by a slight modification of the wave equation, and the type of uniform stability that we observe for the wave equation also is manifest here. This is striking for many reasons. First, the delicate ill-posedness behavior of the original Birkhoff-Rott equation disappears at the linear level. This means that the most important terms for describing sheet breakdown and singularity formation in this case must be non-linear, which the authors explore in [34]. Furthermore, to our knowledge this is the first known example of a vortex sheet which is even linearly stable (within the class of perturbations of the sheet itself, as opposed to velocity perturbations).

As an example, the real cosine perturbation initially defined by $f_1(\alpha) = a\cos k\alpha,\ f_2(\alpha) = 0$ yields the stable travelling wave solution

$$\xi(\alpha,t) = a\cos(k(\alpha - t/2)) + i\frac{2a}{k}\left(\sin(k\alpha) - \sin(k(\alpha - t/2))\right). \tag{2.61}$$

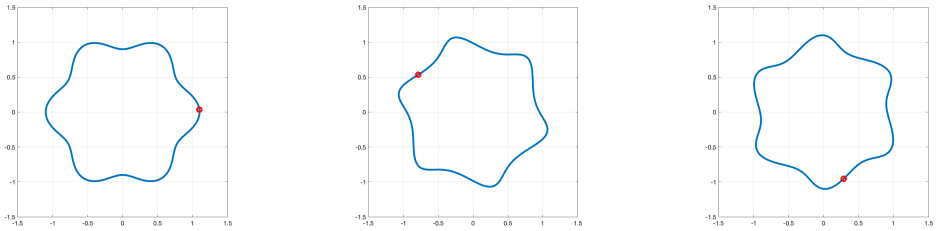

(a) $t = 0$ (b) $t = 5$ (c) $t = 10$

Figure 1: Stable evolution of the linearized problem.

Figure 1 plots the travelling wave solution given by the combination of the steady solution with (2.60) for the initial condition $f_1(\alpha) = 0.1\cos 6\alpha,\ f_2(\alpha) = 0$. The overall rotation of the vortex sheet can be seen by the red tracking point. The wave travels around the steady solution and its shape fluctuates slightly, but it remains stable.

Remark 2.3. *It is also possible to evaluate the stability of the linear evolution problem by writing the perturbation as*

$$\xi(\alpha, t) = \sum_{k\in\mathbb{Z}} (B_k(t) + iC_k(t))e^{i(k\alpha + t/2)}, \tag{2.62}$$

where B_k and C_k are real Fourier coefficients. We notice that by assuming a slightly different form for the perturbation, Fourier coupling shifts to the $\pm k$ modes, as for the flat sheet. We reiterate that the absence of such coupling is the critical error made by [32, 42]. We can then write (2.54) *as*

$$\frac{d}{dt}\begin{bmatrix} B_k \\ C_k \\ B_{-k} \\ C_{-k} \end{bmatrix} = \begin{bmatrix} 0 & 1/2 & 0 & -(k+1)/2 \\ -1/2 & 0 & -(k+1)/2 & 0 \\ 0 & (k-1)/2 & 0 & 1/2 \\ (k-1)/2 & 0 & -1/2 & 0 \end{bmatrix} \begin{bmatrix} B_k \\ C_k \\ B_{-k} \\ C_{-k} \end{bmatrix}. \tag{2.63}$$

The eigenvalues associated with this system are $\lambda = \pm ik/2$, each with geometric multiplicity of two. As in the case of an additive perturbation, the matrix can be completely diagonalized about these eigenvalues, implying stable oscillation of the perturbation about the circular vortex sheet. This approach mirrors that of the Kelvin-Helmholtz instability on a flat sheet and our earlier approach to the additive perturbation, but the solution via characteristics provides more direct insight.

Finally, it is tempting to think that the flat sheet should be attainable as a limit of infinitely large circular sheets. We notice that this is not the case for at least one clear reason: the principal value in the flat sheet must accommodate cancellations at spatial infinity that are not present in the circular sheet. Furthermore, the circular sheet also does add an additional implicit constraint that the velocities on the interior of the shear interface are zero: otherwise there is an implicit vortex point at the origin. This type of constraint is not relevant in the case of the flat sheet, as one can add a globally constant flow in the direction of the interface to attain any desired velocity without changing the strength of the vortex sheet.

3 Generalized Birkhoff-Rott

The explicit formulas in the previous section are compelling, but do not correspond to the previously observed instability of circular sheets in numerical simulations [45]. Of course such instability could be solely a non-linear effect, but in our experience this instability is rather robust in simulation: hence in this section we examine the stability of the circular sheet under a more general class of models including those which are commonly used in numerical simulations (and in other analytical studies).

In particular, we will consider a class of generalized Birkhoff-Rott equations which use a regularizing kernel to avoid the singularity of the classical Birkhoff-Rott equation. We will consider curve evolution equations of the form

$$\partial_t z^*(\alpha, t) = \frac{1}{2\pi i} \text{P.V.} \int K(z(\alpha, t), z(\beta, t))\, d\beta, \tag{3.1}$$

where the kernel K can be written as

$$K(z_1, z_2) = \frac{(z_1 - z_2)^*}{f(|z_1 - z_2|)}, \tag{3.2}$$

where f is a real-valued, non-negative function. The assumption that the kernel has $z_1^* - z_2^*$ in the numerator guarantees that the velocity field is purely rotational (i.e. incompressible), and the fact that f only depends upon the distance between z_1, z_2 relates to a type of isotropy of the velocities induced by the "vorticity". Kernels of this form include the following:

- When $K(z_1, z_2) = \frac{1}{z_1 - z_2}$ we have that $f(|z_1 - z_2|) = |z_1 - z_2|^2$, and then Equation (3.1) corresponds to the classical Birkhoff-Rott equation.
- When $K(z_1, z_2) = \frac{(z_1 - z_2)^*}{|z_1 - z_2|^2 + \delta^2}$ for some $\delta > 0$ then Equation (3.1) corresponds to the popular regularized numerical methods proposed by [21]. These are also the kernels reported in [45].
- When $K(z_1, z_2) = \frac{1}{z_1 - z_2}\left(1 - \frac{|z_1 - z_2|}{\alpha} K_1\left(\frac{|z_1 - z_2|}{\alpha}\right)\right)$, where K_1 is a modified Bessel function, then this corresponds to the α-Birkhoff-Rott equation proposed in [4]. This equation can also be obtained by replacing the Biot-Savart law $\nabla^\perp \Delta^{-1} \omega = v$ with $(I - \delta^2 \Delta)^{-1} \nabla^\perp \Delta^{-1} \omega = v$, see Section 2 in [4] for details.
- One could also consider power-law forms of Birkhoff-Rott where $K(z_1, z_2) = \frac{(z_1 - z_2)^*}{|z_1 + z_2|^{2-\delta}}$, with $\delta > 0$.

Each of these essentially corresponds to a different choice of kernel in the Biot-Savart law. Here we restrict our attention to purely incompressible flows: this rules out the aggregation type kernels previously considered in [45].

3.1 Linearized Instability for Circular Vortex Sheets Under General Kernels

We now consider the linear evolution problem for a circular vortex sheet under general kernels which are of the form (3.2). For analytical convenience, and motivated by the kernels used in practice, we will make the additional assumption that $f : (0, 3) \to (0, \infty)$ is a C^1 function satisfying, for some $\kappa > 1/2$,

$$\lim_{y \to 0} \frac{1}{y^\kappa} \int_0^y \left| \frac{1}{f(z)} \right| dz < \infty, \qquad \lim_{y \to 0} \frac{1}{y^\kappa} \int_0^y \left| \frac{z f'(z)}{f^2(z)} \right| dz < \infty. \tag{3.3}$$

We notice that if f is uniformly bounded away from zero then we may take $\kappa = 1$. We also notice that since $f \in C^1$ and maps into $(0, \infty)$ the the previous assumption also implies integrability of both $\frac{1}{f}$ and $\frac{zf'}{f^2}$ on $(0, 3)$. Finally, we mention that the domain $(0, 3)$ is for convenience, since the input of f, f' is always $|e^{i\alpha} - e^{i\beta}|$, which takes values between 0 and 2.

Under these assumptions, we may write the generalized Birkhoff-Rott Equation (3.1) as

$$\partial_t z^*(\alpha, t) = \frac{1}{2\pi i} \int \frac{z^*(\alpha) - z^*(\beta)}{f(|z(\alpha) - z(\beta)|)} d\beta, \tag{3.4}$$

where we may safely remove the principal value since the integrals are now finite. We note that by making the assumption (3.3) we have ruled out the classical Birkhoff-Rott case, but still permit the kernels used in [23] and [4], as the former is strictly bounded away from zero and the latter only has logarithmic growth near zero.

As in our analysis of the classical Birkhoff-Rott equation in the previous subsection, we consider the evolution of the perturbed circular vortex sheet described by $z(\alpha, t) = e^{i(\alpha + Ct)}(1 + \xi(\alpha))$ for $\alpha \in [0, 2\pi]$ and some constant C (with a value given below). Equation (3.1) then becomes

$$\partial_t (e^{i(\alpha+Ct)}(1 + \xi(\alpha))) = \frac{-e^{iCt}}{2\pi i} \int_0^{2\pi} \frac{e^{i\alpha}(1 + \xi(\alpha)) - e^{i\beta}(1 + \xi(\beta))}{f(|e^{i\alpha}(1 + \xi(\alpha)) - e^{i\beta}(1 + \xi(\beta))|)} d\beta. \tag{3.5}$$

Assuming that ξ is small, we Taylor expand the integrand about the steady solution ($\xi \equiv 0$) to obtain

$$\partial_t (e^{i(\alpha+Ct)}(1 + \xi(\alpha))) \approx \frac{-e^{iCt}}{2\pi i} \int_0^{2\pi} \frac{e^{i\alpha} - e^{i\beta}}{f(|e^{i\alpha} - e^{i\beta}|)} + \frac{e^{i\alpha}\xi(\alpha) - e^{i\beta}\xi(\beta)}{f(|e^{i\alpha} - e^{i\beta}|)} \tag{3.6}$$

$$- \frac{f'(|e^{i\alpha} - e^{i\beta}|)(e^{i\alpha} - e^{i\beta}) Re((e^{i\alpha}\xi(\alpha) - e^{i\beta}\xi(\beta))(e^{-i\alpha} - e^{-i\beta}))}{f(|e^{i\alpha} - e^{i\beta}|)^2 |e^{i\alpha} - e^{i\beta}|} d\beta. \tag{3.7}$$

Here we notice that in the second term for the chain rule we needed to use the fact that the derivative of $|\cdot|$ at a point z in the direction w is written in complex variables as $\frac{Re(z^* w)}{|z|}$, as can readily be verified by rewriting the complex numbers as vectors in $\mathbb{R}^2$.

The first term corresponds to the steady case where $\xi \equiv 0$, i.e.

$$\partial_t e^{i(\alpha+Ct)} = iCe^{i(\alpha+Ct)} = \frac{-e^{i(\alpha+Ct)}}{2\pi i} \int_0^{2\pi} \frac{1 - e^{i(\beta-\alpha)}}{f(|e^{i\alpha} - e^{i\beta}|)} d\beta. \tag{3.8}$$

This gives us a formula for C (which is well-defined by Assumption (3.3)), namely

$$C = \frac{1}{2\pi} \int_0^{2\pi} \frac{1 - e^{i(\beta-\alpha)}}{f(|e^{i\alpha} - e^{i\beta}|)} d\beta = \frac{1}{2\pi} \int_0^{2\pi} \frac{1 - \cos(\tilde{\beta})}{f(|1 - e^{i\tilde{\beta}}|)} d\tilde{\beta} \in \mathbb{R}, \tag{3.9}$$

where we have used the oddness of sine and the 2π-periodicity of the argument of f. Returning to our computation, we see that the linearized equation is given by

$$\partial_t \xi(\alpha, t) = -iC\xi(\alpha) - \frac{1}{2\pi i} \int_0^{2\pi} \frac{\xi(\alpha) - e^{i(\beta-\alpha)}\xi(\beta)}{f} d\beta \tag{3.10}$$

$$+ \frac{1}{2\pi i} \int_0^{2\pi} \frac{f'}{f^2} \frac{(1 - e^{i(\beta-\alpha)}) Re((\xi(\alpha) - e^{i(\beta-\alpha)}\xi(\beta))(1 - e^{-i(\beta-\alpha)}))}{|e^{i\alpha} - e^{i\beta}|} d\beta, \tag{3.11}$$

where the argument of f and f' is $|e^{i\alpha} - e^{i\beta}|$ (which we omit for brevity). We notice that, again using the change of variables $\tilde{\beta} = \beta - \alpha$ and the oddness of sine, we may simplify this somewhat to obtain

$$\partial_t \xi(\alpha, t) = iM_1\xi(\alpha) + iM_2 Re(\xi(\alpha)) + M_3 Im(\xi(\alpha)) \tag{3.12}$$

$$+ \frac{1}{2\pi i}\int_0^{2\pi} \frac{e^{i(\tilde{\beta})}\xi(\tilde{\beta}+\alpha)}{f(|1-e^{i\tilde{\beta}}|)}\, d\tilde{\beta} \tag{3.13}$$

$$- \frac{1}{2\pi i}\int_0^{2\pi} \frac{f'(|1-e^{i\tilde{\beta}}|)(1-e^{i\tilde{\beta}})Re((e^{i\tilde{\beta}}\xi(\tilde{\beta}+\alpha))(1-e^{-i\tilde{\beta}}))}{f(|1-e^{i\tilde{\beta}}|)^2|1-e^{i\tilde{\beta}}|}\, d\tilde{\beta}, \tag{3.14}$$

with

$$M_1 = \frac{1}{2\pi}\int_0^{2\pi} \frac{1}{f(|1-e^{i\tilde{\beta}}|)} d\beta - C = \frac{1}{2\pi}\int_0^{2\pi} \frac{\cos(\tilde{\beta})}{f(|1-e^{i\tilde{\beta}}|)}\, d\tilde{\beta} \tag{3.15}$$

$$M_2 = -\frac{1}{2\pi}\int_0^{2\pi} \frac{f'(|1-e^{i\tilde{\beta}}|)(1-\cos(\tilde{\beta}))^2}{f(|1-e^{i\tilde{\beta}}|)^2|1-e^{i\tilde{\beta}}|}\, d\tilde{\beta} \tag{3.16}$$

$$M_3 = \frac{1}{2\pi}\int_0^{2\pi} \frac{f'(|1-e^{i\tilde{\beta}}|)\sin^2(\tilde{\beta}))}{f(|1-e^{i\tilde{\beta}}|)^2|1-e^{i\tilde{\beta}}|}\, d\tilde{\beta}. \tag{3.17}$$

We now suppose that

$$\xi(\alpha, t) = (a_k(t) + ib_k(t))\cos(k\alpha) + (c_k(t) + id_k(t))\sin(k\alpha), \tag{3.18}$$

where $k \in \mathbb{N}$ and a_k, b_k, c_k, and d_k are real Fourier coefficients. We use a sine/cosine series instead of complex exponentials due to the presence of the real part in the formula. After expanding using trigonometric identities, we can rewrite the linearized equation as the following system

$$\frac{d}{dt}\begin{bmatrix} a_k \\ b_k \\ c_k \\ d_k \end{bmatrix} = \begin{bmatrix} S & cI_2 \\ -cI_2 & S \end{bmatrix}\begin{bmatrix} a_k \\ b_k \\ c_k \\ d_k \end{bmatrix} \tag{3.19}$$

where

$$S = \begin{bmatrix} 0 & -M_1 + M_3 + M_4 + M_5 \\ M_1 + M_2 - M_4 + M_6 & 0 \end{bmatrix} \tag{3.20}$$

with

$$M_4 = \frac{1}{2\pi}\int_0^{2\pi} \frac{\cos(k\tilde{\beta})\cos(\tilde{\beta})}{f(|1-e^{i\tilde{\beta}}|)}\, d\tilde{\beta}, \tag{3.21}$$

$$M_5 = -\frac{1}{2\pi}\int_0^{2\pi} \frac{f'(|1-e^{i\tilde{\beta}}|)\cos(k\tilde{\beta})\sin^2(\tilde{\beta})}{f(|1-e^{i\tilde{\beta}}|)^2|1-e^{i\tilde{\beta}}|}\, d\tilde{\beta}, \tag{3.22}$$

$$M_6 = -\frac{1}{2\pi}\int_0^{2\pi} \frac{f'(|1-e^{i\tilde{\beta}}|)\cos(k\tilde{\beta})(1-\cos(\tilde{\beta}))^2}{f(|1-e^{i\tilde{\beta}}|)^2|1-e^{i\tilde{\beta}}|}\, d\tilde{\beta}, \tag{3.23}$$

and

$$c = \frac{1}{2\pi}\int_0^{2\pi} \frac{\sin(k\tilde{\beta})\sin(\tilde{\beta})}{f(|1-e^{i\tilde{\beta}}|)}\, d\tilde{\beta} - \frac{1}{2\pi}\int_0^{2\pi} \frac{f'(|1-e^{i\tilde{\beta}}|)\sin(k\tilde{\beta})\sin(\tilde{\beta})(1-\cos(\tilde{\beta}))}{f(|1-e^{i\tilde{\beta}}|)^2}\, d\tilde{\beta}. \tag{3.24}$$

The matrix in (3.19) provides a tool with which we can test the linearized stability of a given regularizing kernel. To this end, we define the quantity $m_k := (-M_1 + M_3 + M_4 + M_5)(M_1 + M_2 - M_4 + M_6)$, where the constants M_i are defined above, for any $k \in \mathbb{N}$.

There is a useful relationship between the eigenvalues of S and those of the matrix in (3.19). The eigenvalues of S are easily computed as $\lambda_s = \pm\sqrt{m_k}$. If $m_k \neq 0$ we can then diagonalize S as

$$\hat{S} = \begin{bmatrix} \lambda_s^1 & 0 \\ 0 & \lambda_s^2 \end{bmatrix}. \tag{3.25}$$

By the block structure of the matrix in (3.19), we then compute

$$\det \begin{pmatrix} \hat{S} - \lambda I_2 & cI_2 \\ -cI_2 & \hat{S} - \lambda I_2 \end{pmatrix} = \det((\hat{S} - \lambda I_2)^2 + c^2 I_2) \tag{3.26}$$

$$= \det \begin{pmatrix} (\lambda_s^1 - \lambda)^2 + c^2 & 0 \\ 0 & (\lambda_s^2 - \lambda)^2 + c^2 \end{pmatrix}, \tag{3.27}$$

which yields eigenvalues $\lambda = \pm\sqrt{m_k} \pm ic$. We first notice that if $m_k < 0$, then the eigenvalues of S are purely imaginary, and the eigenvalues of (3.19) are purely imaginary as well. If c is nonzero these eigenvalues are distinct, and if c is equal to zero then the blocks of S are completely decoupled so the larger matrix can be fully diagonalized. Whether or not $c = 0$, if $m_k < 0$ we have stability of the system (3.19) and therefore for the linearized evolution problem of the generalized Birkhoff-Rott Equation (3.1). In this first case (i.e. $m_k < 0$, uniformly in k), the change of variables which diagonalizes the system matrix in (3.19) will be uniformly invertible. As the sine and cosine series provides an orthonormal basis of L^2, this implies that in this case there exists a norm which is equivalent to L^2 under which the dynamics are stable, which then implies that the dynamics are also stable in L^2.

In the case that $m_k = 0$, the matrix in (3.19) has eigenvalues $\lambda = \pm ic$ each with geometric multiplicity of two, but yields the nontrivial Jordan form

$$\begin{bmatrix} -ic & 1 & 0 & 0 \\ 0 & -ic & 0 & 0 \\ 0 & 0 & ic & 1 \\ 0 & 0 & 0 & ic \end{bmatrix}, \tag{3.28}$$

implying unstable growth of the perturbation like t. Finally, we note that if $m_k > 0$ (for any k), then the eigenvalues of S are purely real, so some of the eigenvalues of (3.19) have a positive real part, again implying instability of the linear evolution problem. We summarize the above arguments as a pair of propositions which characterize the linear stability of the generalized Birkhoff-Rott Equation (3.1).

Proposition 3.1. *Define m_k as above for any $k \in \mathbb{N}$. If there exists an M so that $m_k < M < 0$ for all k, then the generalized Birkhoff-Rott equation is stable in $L^2(\mathbb{S})$ when linearized about the circular steady state.*

Proposition 3.2. *Define m_k as above for any $k \in \mathbb{N}$. If $m_k \geq 0$ for any k, then the generalized Birkhoff-Rott equation is unstable in $L^2(\mathbb{S})$ when linearized about the circular steady state.*

These results provide a direct characterization of linear instability/stability for general kernels. This characterization is made possible by the relatively simple block structure of the matrix associated with each Fourier mode, allowing us to reduce checking stability of any given mode to computing a single, explicit constant.

In many cases it may be challenging compute m_k without resorting to numerical integration. Furthermore, the previous propositions did not directly account for the situation where $m_k \to 0$. In fact the popular kernel proposed in [21] has an exact integral identity that implies that $m_k \to 0$, independently of δ. In this case it turns out that we can still obtain a linear instability result (with growth of the operator norm of order t), which we now state and prove.

Proposition 3.3. *The Krasny regularization of the generalized Birkhoff-Rott kernel is defined by*

$$K(z_1, z_2) = \frac{(z_1 - z_2)^*}{|z_1 - z_2|^2 + \delta^2} \tag{3.29}$$

for some $\delta > 0$. Under this kernel regularization, the generalized Birkhoff-Rott equation is unstable when linearized about the circular steady state, in the sense that the operator norm of the solution mapping grows at a rate proportional to (at least) t in $L^2(\mathbb{S})$.

Proof. The Krasny kernel regularization may be written as

$$\frac{(z_1 - z_2)^*}{f(|z_1 - z_2|)} \tag{3.30}$$

where $f(|z_1 - z_2|) = |z_1 - z_2|^2 + \delta^2$. We consider the evolution of a circular vortex sheet with a high-frequency perturbation, i.e. we define ξ by Equation (3.18) and take $k \to \infty$. Under integrability assumptions on f the terms $M_4,\ M_5,\ M_6$, and c all go to zero as $k \to \infty$. We are then left with $\lim_{k\to\infty} m_k =: m_\infty = (-M_1 + M_3)(M_1 + M_2)$.

To verify the asymptotic behavior of Equation (3.19) at high modes, we note that this is a linear evolution problem of the form $\frac{d}{dt}x_k(t) = A_k x_k(t)$, where the matrix A_k is constant for a given k. It can be shown that for a fixed $t \in \mathbb{R}$, the matrix exponential $e^{A_k t} \to e^{A_\infty t}$ and thus the solution $x_k(t) \to x_\infty(t)$ as $A_k \to A_\infty$.

The integral $M_3 - M_1$ can be evaluated using trigonometric identities and substitutions as

$$\begin{aligned}
M_3 - M_1 &= \frac{1}{2\pi}\int_0^{2\pi} \frac{f'(|1 - e^{i\tilde\beta}|)}{f(|1 - e^{i\tilde\beta}|)^2}\frac{\sin^2(\tilde\beta)}{|1 - e^{i\tilde\beta}|} - \frac{\cos(\tilde\beta)}{f(|1 - e^{i\tilde\beta}|)}d\tilde\beta && (3.31)\\
&= \frac{1}{2\pi}\int_0^{2\pi} \frac{2\sin^2(\tilde\beta)}{(|1 - e^{i\tilde\beta}|^2 + \delta^2)^2} - \frac{\cos(\tilde\beta)}{|1 - e^{i\tilde\beta}|^2 + \delta^2}d\tilde\beta && (3.32)\\
&= \frac{1}{2\pi}\int_0^{2\pi} \frac{2 - (\delta^2 + 2)\cos(\tilde\beta)}{(2(1 - \cos(\tilde\beta)) + \delta^2)^2}d\tilde\beta && (3.33)\\
&= \frac{\sin(\tilde\beta)}{2\pi(2\cos(\tilde\beta) - (\delta^2 + 2))}\Bigg|_0^{2\pi} = 0. && (3.34)
\end{aligned}$$

We then have $m_\infty = 0$, which is the second case discussed in the section preceding Proposition 3.2. We conclude that the linear evolution problem is unstable for asymptotically high modes, in the sense that $\lim_{k\to\infty} \|e^{A_k}t\| \to Ct$ for any fixed t, where here A_k is the matrix associated with the k-th terms in the sine/cosine expansion, $\|\cdot\|$ here means the matrix norm, and C is independent of t. The fact that the Fourier series provides an orthonormal basis in L^2 then proves the desired result. □

For checking the stability of other kernel regularizations, it is useful to make a few further remarks about the structure of the matrix in (3.19):

i) Under integrability assumptions on f the terms $M_4,\ M_5,\ M_6$, and c all go to zero as $k \to \infty$. Hence, although we in principle need to compute the sign difference of the off-diagonals of S for all integer values of k, in practice a finite number of k will suffice.

ii) The off diagonal entries have terms $\pm(M_1 - M_4)$, so one can hope that these terms dominate the sign comparison. Indeed, M_1 has an integrand $\frac{\cos(\beta)}{f}$, and so the large values of $1/f$ near zero are not cancelled; a similar argument holds for M_4. Cancellation near zero does occur for all of the other terms.

4 Numerical Methods and Simulations

The analytical study of vortex sheet evolution is often limited by the approximations inherent in linearized analysis. Well-established numerical methods can help us understand nonlinear vortex sheet evolution up to and beyond the development of singularity [22, 23], for example illustrating the roll-up of Kelvin-Helmholtz on a flat sheet. Indeed, previous research has already demonstrated that circular vortex sheets exhibit spiral roll-up reminiscent of the Kelvin-Helmholtz instability in numerical simulations [45, 43]. Here we will briefly discuss numerical methods for incompressible and inviscid vortex sheet dynamics, and give some some examples of the Kelvin-Helmholtz instability on circular sheets. This section is intended to demonstrate the gap between the delicate linear stability of the circular vortex sheet (Theorem 2.2) and the regularized nonlinear instability.

4.1 Regularized Computational Method

The point vortex method is one such technique for computing vortex sheet evolution. Given a vortex sheet parameterized by vorticity, we consider the discretization $z_j = z(\alpha_j, t)$, $j = 1, \ldots, N$. By approximating the sheet using point vortices at the points z_j, we can derive the system of ODEs [24]

$$\frac{dz_j^*}{dt} = \frac{1}{2\pi i} \sum_{k=1, k\neq j}^{N} K(z_j, z_k) w_k, \tag{4.1}$$

where the w_k are quadrature weights for the spatial discretization. A natural choice of kernel is

$$K(z_1, z_2) = \frac{1}{z_1 - z_2}, \tag{4.2}$$

which is the kernel associated with the classical Birkhoff-Rott Equation (1.4), and in the discrete case it views vorticity as concentrated exactly at each z_j. Before the time of singularity development [30], the point vortex method with this kernel converges towards the Birkhoff-Rott solution as $N \to \infty$ [22]. After roll-up begins, the numerical evolution becomes unstable and kernel must be regularized to proceed further in time. One such regularization is the Krasny kernel [21]

$$K(z_1, z_2) = \frac{1}{z_1 - z_2} \frac{|z_1 - z_2|^2}{|z_1 - z_2|^2 + \delta^2}, \tag{4.3}$$

which can be conveniently rewritten using properties of complex numbers as

$$K(z_1, z_2) = \frac{(z_1 - z_2)^*}{|z_1 - z_2|^2 + \delta^2}. \tag{4.4}$$

Here δ is a smoothing parameter which moderates the singularity in the Cauchy kernel; its presence corresponds to vorticity spread over small areas around each z_j. The Krasny kernel is the focus of Proposition 3.3. There are a variety of other options for regularized kernels corresponding to the generalized Birkhoff-Rott Equation (3.1). We will focus on the Krasny kernel here, but another interesting example is the α-regularization studied by [4].

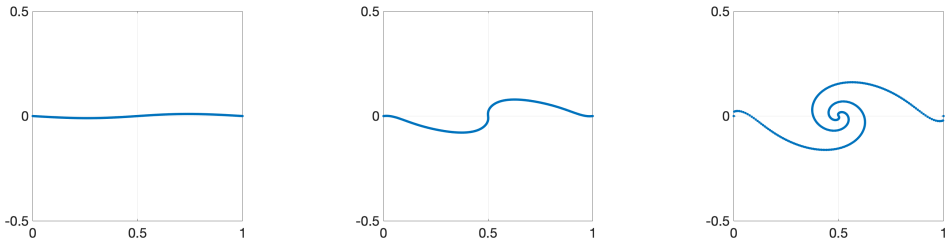

(a) $t = 0$ (b) $t = 1$ (c) $t = 1.5$

Figure 2: The Kelvin-Helmholtz instability on a flat sheet.

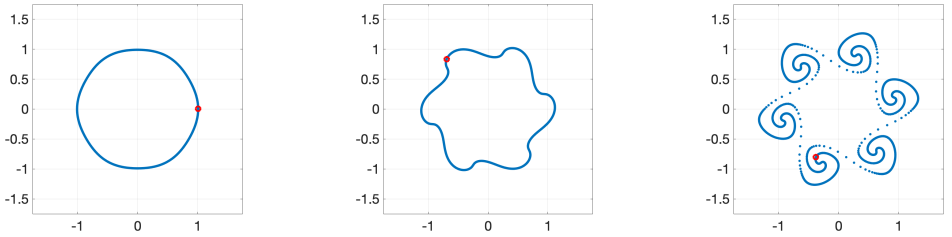

(a) $t = 0$ (b) $t = 5$ (c) $t = 10$

Figure 3: Nonlinear evolution of a perturbed circular vortex sheet.

4.2 Nonlinear Simulation

To illustrate the effectiveness of the regularized point-vortex method, we first use (4.4) to simulate the Kelvin-Helmholtz instability on an initially flat sheet with a periodic perturbation of the form $z(\alpha, 0) = \alpha + \xi(\alpha, 0)$. We apply periodic boundary conditions, implemented as described in [21]. Mirroring that study, we use $\delta = 0.25$ and $N = 400$ with the initial condition $z(\alpha, 0) = \alpha + 0.01 \sin(2\pi\alpha) - i0.01 \sin(2\pi\alpha)$ for $\alpha \in [0, 1]$. Figure 2 shows the computed evolution.

The roll-up observed here is characteristic of the Kelvin-Helmholtz instability [11, 24] and is a classical problem in computing vortex sheet motion. It is important to note that although linearized analysis of the flat vortex sheet indicates some strong instability, it does not capture a mechanism for the roll-up observed numerically and experimentally. The influence of the smoothing parameter δ is discussed in detail in [21]; smaller values of δ lead to an increased number of turns observed in the core of the roll-up at a given time, and the kernel approaches that of the classical Birkhoff-Rott equation, but there are challenges at finite precision.

We can similarly use the regularized point-vortex method with the Krasny kernel (4.4) to simulate the evolution of an initially circular vortex sheet with a periodic perturbation of the form $z(\alpha, 0) = e^{i\alpha}(1 + \xi(\alpha, 0))$. Since the geometry is a closed contour, there is no need to apply a periodic boundary condition and the numeric evolution can be viewed purely as an initial value problem. We use $\delta = 0.25$, $N = 1600$, and the initial condition $z(\alpha, 0) = e^{i\alpha}(1 + 0.01 \cos(6\alpha))$. Figure 3 shows the computed evolution.

The perturbed circular vortex sheet exhibits nonlinear instability by rolling up much like the Kelvin-Helmholtz instability on a flat vortex sheet, albeit more slowly. In particular, roll-up

solutions on both circular and flat sheets exhibit wave breaking phenomena, in the sense that solutions of the nonlinear equations cease to be the graph of a (real-valued) function ξ. This instability is expected from our analysis of the generalized Birkhoff-Rott equation in Section 3. In particular, Proposition 3.3 proved linearized instability for the Krasny kernel under high-frequency perturbations. Here, we observe nonlinear instability under a relatively low-frequency perturbation. Because of issues with finite precision, it is difficult to isolate linear instability due to regularization of the kernel (Proposition 3.3) from nonlinear contributions to instability [34].

5 Experimental Demonstration

We use a simple experiment to qualitatively demonstrate the real development of instability on a circular shear layer, and observe a striking similarity to numerical demonstrations.

Our experiment was initially motivated by the observation of wave-breaking instability in a cup of coffee, shown in Figure 4. These images were obtained by stirring the coffee in smooth circular motions, and then pouring cream into the center of the cup. When viewed from above, this forms a rough approximation of a circular shear layer because the cream has no angular velocity. Wave-breaking instabilities form and reform at the shear interface until the cream is diffused. This phenomenon cannot be reduced to two dimensions and the density is variable, so any application of our previous analysis is tenuous. Nonetheless, these images motivated the design of a controlled laboratory experiment which attempts to isolate circular vortex sheet instability.

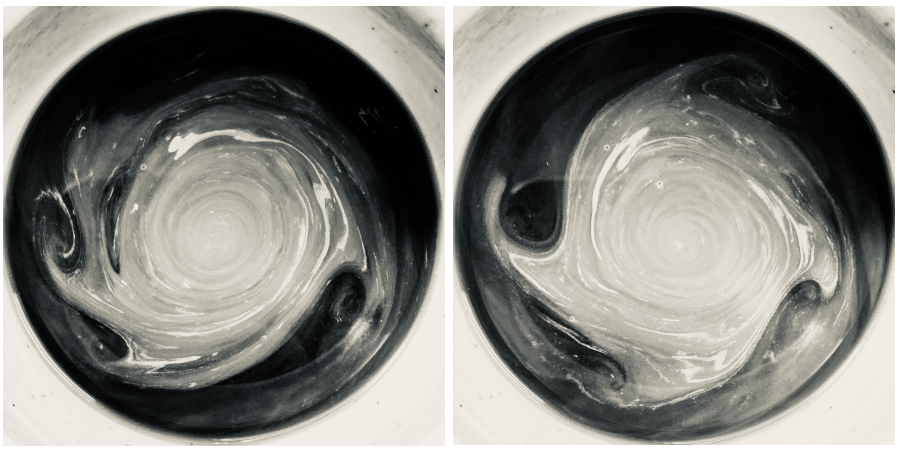

(a) Irregular wave-breaking instability. (b) Symmetric wave-breaking instability.

Figure 4: Development of wave-breaking instability in a coffee cup. Various symmetric and asymmetric patterns of vortices tend to form, smooth out, and reform until the cream is diffused and/or the angular momentum of the coffee dissipates.

Existing research has shown that under the influence of centrifugal forces, a stable circular shear layer may be observed with steady polygonal patterns of vortices [1, 16]. This contour resembles geophysical flows like Saturn's North Polar Hexagon, and roughly corresponds to our perturbed circular vortex sheet. Since our analysis is at a local scale of fluid behavior and neglected centrifugal effects like the rotation of a planet, it is reasonable to assume that the

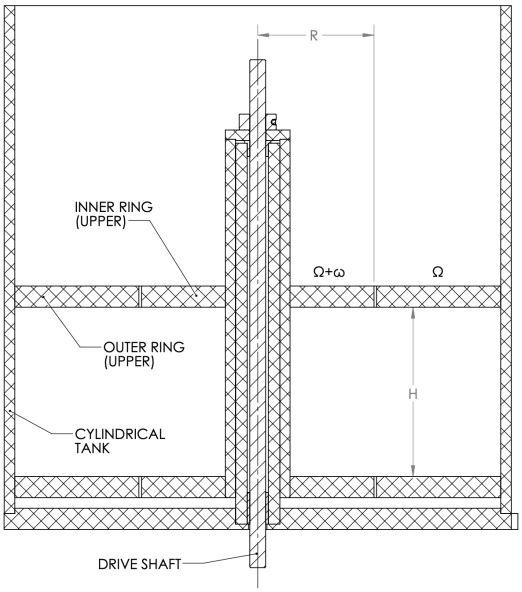

Figure 5: Experimental setup, with test section height H and split radius at R.

presence of background rotation is stabilizing. Such an effect also explains why [41] obtained steady polygonal patterns. Thus, our procedure will isolate the development of instability by removing background rotation once a steady flow is established.

Of course, inviscid experiments cannot be truly realized in a physical setting, and so the inviscid instability of a circular vortex sheet is impossible to isolate. The shear layer studied here is a reasonable approximation, but it is different from the idealized circular vortex sheet due to the critical role of viscosity, and some degree of vertical transport. Perhaps most importantly, the limited size of the experimental setup and viscous interaction with the outer wall alters the flow due to boundary layer effects, and creates vorticity away from the shear layer under consideration. Despite these confounding factors, the experiment presented here bears much resemblance to the numerical simulations carried out in Section 4, and demonstrates the persistence of the Kelvin-Helmholtz instability in real shear flows.

5.1 Experimental Design

The experimental setup broadly consists of a large acrylic cylinder with a differentially rotating core. The test section is defined by acrylic annuli offset at height H. The outer annuli are fixed to the wall of the tank. At the upper and lower boundary of the test section, two inner annuli of radius R rotate with the central core at speed ω, driven by a motor underneath the tank. The cylinder is filled with water to a level slightly above the upper annuli. Figure 5 shows a vertical cross-section.

Placing the experimental setup on a variable speed turntable permits the outer section to rotate at speed Ω and the inner section at speed $\Omega + \omega$, establishing a vertical shear layer between the flow regions at radius R. The parameters used to describe the dynamics are the Ekman number $E = \frac{\nu}{\overline{\Omega} H^2}$ and Rossby number $Ro = \frac{R\omega}{2\overline{\Omega} H}$. In their definition, ν is the kinematic viscosity of the working fluid and $\overline{\Omega}$ is the mean fluid velocity, calculated using the area ratio of

Variable	Value/range
Overall dia.	29.21 cm.
Inner core rad.	1.91 cm.
H	5.23 cm.
R	6.99 cm.
ν	0.0103 cm^2/s (water at 20°C)
Ω	$-8.0 \leq \Omega \leq 8.0$ rad/s $\pm 0.05\%$
ω	0.31 or 0.63 rad/s $\pm 0.05\%$

Table 1: Experimental variables.

inner and outer annuli.

For $\Omega \neq 0$ and $\omega \neq 0$, viscous forces lead to the formation of horizontal shear layers, called Ekman layers, of radius R against the upper and lower boundaries of the test section. The thickness of the Ekman layers are proportional to $E^{1/2}$ and $E^{1/3}$. To balance radial mass flux, Ekman layers drive some degree of vertical velocity. A vertically uniform Stewartson shear layer of height H and thickness $L = (E/4)^{1/4}H$ forms at the split radius; viscosity is important here, but for sufficiently small E this cylindrical shear layer approximates the circular vortex sheet when viewed from above [16, 44].

Our experiment employs the values presented in Table 1; the geometry is a scaled version of that used in [1, 16], which met our experimental constraints and allows a larger value of H to permit visualization of the dynamics outside the viscosity-dominated Ekman layer.

By varying Ω and ω, we established steady and approximately circular contours with symmetric polygonal patterns of m vortices. A thorough regime diagram over Ro and E has been constructed by both [1] and [16] which shows how different parameter choices lead to different steady state values of m in the case of background rotation. Our goal is to study the development of instability for certain parameter combinations, rather than to characterize steady states. We used the background rotation Ω to stabilize the circular shear layer at some value of m, so the flow structure resembles a physical perturbation of the circular solution to Birkhoff-Rott when viewed from above. After observing the steady state, background rotation was removed while keeping the velocity differential ω constant, triggering the onset of instability at inflection points.

We conducted all experimental trials using $\omega = 0.31$ or 0.63 rad/s and various values of Ω. For each trial, the test setup was filled with water to slightly above the upper annuli. The motors were turned on and their speeds measured with a handheld tachometer, which has a relative precision of $\pm 0.05\%$. The flow was then allowed to equilibriate for 30 minutes. At this point a steady flow had been established, so ω and Ω were measured again and visualization could proceed. The flow was visualized using fluorescein dye, which was injected by hand at the split radius. Though dye injection introduced some turbulence, the mean flow was still well-organized.

5.2 Experimental Results

In this section we present qualitative results and compare them with numerical simulation of the inviscid model. A variety of parameter combinations were used in a series of experimental trials, which yielded different polygonal configurations and similar mechanisms of instability development. We will focus our attention on the steady state and development of instability for

Figure 6: Steady state with $Ro = 0.12$ and $E = 1.1 \times 10^{-4}$, $m = 3$ vortices are visible.

(a) $t = 0$s (b) $t = 55$s (c) $t = 127$s

Figure 7: Development of instability for $Ro = 0.12$ and $E = 1.1 \times 10^{-4}$, with $m = 3$.

a particularly illustrative polygonal configuration of vortices with $m = 3$.

This most interesting case is with $\omega = 0.63$ and $\Omega = 3.25$ rad/s, so that $Ro = 0.12$ and $E = 1.1 \times 10^{-4}$. This condition leads to the development of a steady shear layer containing $m = 3$ vortices. Figure 6 shows the steady state from above. This steady state (and all others) are vertically uniform when viewed from the side.

The development of instability under identical conditions to Figure 6 is shown by the series of images in Figure 7.

Numerical simulation of the inviscid analog is shown in Figure 8. Starting with the initial condition $z(\alpha, 0) = e^{i\alpha}(1 + 0.1\cos(3\alpha))$, we implement the regularized point vortex method Equation (4.1) and (4.4) with $\delta = 0.25$ and $N = 800$.

The qualitative similarities between Figures 7 and 8 are striking. The most notable feature is the development of a wave-breaking instability with symmetry $m = 3$ corresponding to the

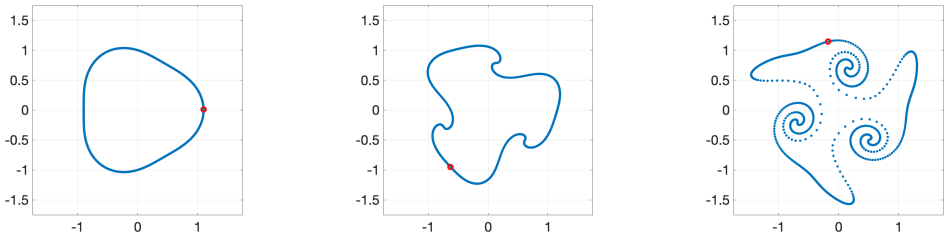

(a) $t = 0$ (b) $t = 5$ (c) $t = 10$

Figure 8: Simulated development of instability for $m = 3$.

symmetry of the initial condition. Behind each rolled-up vortex is an extended tail. Viscous effects are identifiable in the tendency of the real shear layer to increase in diameter over time, and its interaction with the outer wall of the tank. The experiment is nonetheless a compelling demonstration of the Kelvin-Helmholtz instability on a real circular shear layer. The similarity to numerical simulations validates the predictive capability of inviscid stability theory for real shear layer instability.

6 Conclusion

This article shows that the linear stability of the Birkhoff-Rott equation depends strongly on the geometry of the vortex sheet. In Section 2.1, we presented a classical linearized analysis of the Kelvin-Helmholtz instability on a flat sheet. We then explained some conflict with existing research and proved (by several methods) that the Birkhoff-Rott equation is linearly stable for an initially circular geometry. This result suggests that classical linear dynamics are insufficient for explaining the wave-breaking instability observed in numerical simulations, and motivates the study of regularizing kernels for the generalized Birkhoff-Rott equation. In Section 3, we establish a simple criterion for evaluating the linearized stability of circular sheet under regularizing kernels. Counterintuitively, we proved that the addition of a smoothing parameter in the Krasny kernel leads to linearized instability. In Section 4, we presented numerical demonstrations of regularized vortex sheet instability. Finally in Section 5, physical experiments offered a qualitative validation of our numerical model by demonstrating the wave-breaking instability that model predicted.

Acknowledgements

The experimental portion of this research project was made possible by funding from the North Carolina State University Office of Undergraduate Research and the support of Mark Pankow in the Department of Mechanical and Aerospace Engineering. The authors would also like to thank Zach Berger, Ayman Said, and Mohammad Farazmand for many helpful discussions and valuable feedback.

Declaration of interests

The authors report no conflict of interest.

References

[1] Ana C. Barbosa Aguiar et al. "A laboratory model of Saturn's North Polar Hexagon". In: *Icarus* 206 (2010), pp. 755–763.

[2] K. Baines et al. "Saturn's north polar region at depth: The North Polar Hexagon and North Polar Cyclone observed over two years by Cassini/VIMS". In: *Geophys. Res. Abstr.* 11 (Mar. 2009), p. 3375.

[3] Claude Bardos and David Lannes. "Mathematics for 2d interfaces". In: *arXiv preprint arXiv:1005.5329* (2010).

[4] Claude Bardos, Edriss S Titi, and Jasmine S Linshiz. "Global regularity and convergence of a Birkhoff-Rott-α approximation of the dynamics of vortex sheets of the two-dimensional Euler equations". In: *Communications on Pure and Applied Mathematics: A Journal Issued by the Courant Institute of Mathematical Sciences* 63.6 (2010), pp. 697–746.

[5] George Keith Batchelor. *An Introduction to Fluid Dynamics*. Cambridge University Press, 2000.

[6] Ricardo Abreu Blaya, Juan Bory Reyes, and Boris Aleksandrovich Kats. "Cauchy integral and singular integral operator over closed Jordan curves". In: *Monatshefte für Mathematik* 176 (2015), pp. 1–15.

[7] Alberto Bressan and Ryan Murray. "On self-similar solutions to the incompressible Euler equations". In: *Journal of Differential Equations* 269.6 (2020), pp. 5142–5203.

[8] Russel E Caflisch and Oscar F Orellana. "Singular solutions and ill-posedness for the evolution of vortex sheets". In: *SIAM Journal on Mathematical Analysis* 20.2 (1989), pp. 293–307.

[9] Tomasz Cieślak, Piotr Kokocki, and Wojciech S Ożański. "Well-posedness of logarithmic spiral vortex sheets". In: *arXiv preprint arXiv:2110.07543* (2021).

[10] Tomasz Cieślak, Piotr Kokocki, and Wojciech S Ożański. "Existence of nonsymmetric logarithmic spiral vortex sheet solutions to the 2D Euler equations". In: *arXiv preprint arXiv:2207.06056* (2022).

[11] P. G. Drazin and W. H. Reid. *Hydrodynamic Stability*. 2nd ed. Cambridge Mathematical Library. Cambridge University Press, 2004. ISBN: 9780511616938.

[12] Jean Duchon and Raoul Robert. "Global vortex sheet solutions of Euler equations in the plane". In: *Journal of Differential Equations* 73.2 (1988), pp. 215–224.

[13] V Elling and MV Gnann. "Variety of unsymmetric multibranched logarithmic vortex spirals". In: *European Journal of Applied Mathematics* 30.1 (2019), pp. 23–38.

[14] Volker Elling. "Algebraic spiral solutions of the 2d incompressible Euler equations." In: *Bulletin of the Brazilian Mathematical Society* 47.1 (2016).

[15] Volker Elling. "Self-similar 2d Euler solutions with mixed-sign vorticity". In: *Communications in Mathematical Physics* 348.1 (2016), pp. 27–68.

[16] Wolf-Gerrit Fruh and Peter L. Read. "Experiments on a barotropic rotating shear layer. Part 1. Instability and steady vortices". In: *J. Fluid Mech.* 383 (1999), pp. 143–173.

[17] D.A. Godfrey. "A hexagonal feature around Saturn's north pole". In: *Icarus* 76 (1988), pp. 335–356.

[18] Loukas Grafakos. *Modern Fourier Analysis*. Graduate Texts in Mathematics. Springer, 2014, pp. 283–288. ISBN: 978-1-4939-1229-2.

[19] Heinrich Kaden. "Aufwicklung einer unstabilen Unstetigkeitsfläche". In: *Ingenieur-Archiv* 2.2 (1931), pp. 140–168.

[20] Theodore Kolokolnikov et al. "Stability of ring patterns arising from two-dimensional particle interactions". In: *Physical Review E* 84.1 (2011), p. 015203.

[21] R. Krasny. "Desingularization of Periodic Vortex Sheet Roll-up". In: *J. Computational Physics* 65 (1986), pp. 292–313.

[22] Robert Krasny. "A study of singularity formation in a vortex sheet by the point-vortex approximation". In: *Journal of Fluid Mechanics* 167 (1986), pp. 65–93.

[23] Robert Krasny. "Computing vortex sheet motion". In: *Proc. of Inte. Cong. Math., Kyoto, Japan*. 1990, pp. 1573–1583.

[24] Robert Krasny. "Lagrangian Simulation of Vortex Sheet Dynamics". In: (May 2008).

[25] Gilles Lebeau. "Régularité du problème de Kelvin–Helmholtz pour l'équation d'Euler 2d". In: *ESAIM: Control, Optimisation and Calculus of Variations* 8 (2002), pp. 801–825.

[26] Jian-Guo Liu and Zhouping Xin. "Convergence of vortex methods for weak solutions to the 2-D Euler equations with vortex sheet data". In: *Communications on Pure and Applied Mathematics* 48.6 (1995), pp. 611–628.

[27] Milton Lopes Filho, Helena Nussenzveig Lopes, and Steven Schochet. "A criterion for the equivalence of the Birkhoff-Rott and Euler descriptions of vortex sheet evolution". In: *Transactions of the American Mathematical Society* 359.9 (2007), pp. 4125–4142.

[28] Andrew J. Majda and Andrea L. Bertozzi. *Vorticity and Incompressible Flow*. Cambridge Texts in Applied Mathematics. Cambridge University Press, 2002. ISBN: 0 521 63057 6.

[29] Alfons Michalke and Adalbert Timme. "On the inviscid instability of certain two-dimensional vortex-type flows". In: *Journal of Fluid Mechanics* 29.4 (1967), pp. 647–666.

[30] D. W. Moore. "The Spontaneous Appearance of a Singularity in the Shape of an Evolving Vortex Sheet". In: *Proceedings of the Royal Society of London. Series A, Mathematical and Physical Sciences* 365.1720 (1979), pp. 105–119.

[31] D.W. Moore. "Numerical and analytical aspects of Helmholtz instability". In: *Theoretical and applied mechanics*. Elsevier, 1985, pp. 263–274.

[32] D.W. Moore and R. Griffith-Jones. "The stability of an expanding circular vortex sheet". In: *Mathematika* 21 (1974), pp. 128–133.

[33] Max Munk. *Isoperimetrische Aufgaben aus der Theorie des Fluges*. Dieterichsche Universitäts-Buchdruckerei, 1919.

[34] R. Murray and G. Wilcox. "Non-Linear Singularity Formation for Circular Vortex Sheets". In: *Quarterly of Applied Mathematics (accepted)* (2023).

[35] Monika Nitsche, Mark A Taylor, and Robert Krasny. "Comparison of regularizations of vortex sheet motion". In: *Computational Fluid and Solid Mechanics 2003*. Elsevier, 2003, pp. 1062–1065.

[36] D. Pierce. "Photographic evidence of the formation and growth of vorticity behind plates accelerated from rest in still air". In: *Journal of Fluid Mechanics* 11.3 (1961), pp. 460–464. DOI: 10.1017/S0022112061000652.

[37] Bartosz Protas and Takashi Sakajo. "Rotating equilibria of vortex sheets". In: *Physica D: Nonlinear Phenomena* 403 (2020), p. 132286.

[38] Bartosz Protas, Stefan G Llewellyn Smith, and Takashi Sakajo. "Finite rotating and translating vortex sheets". In: *Journal of Fluid Mechanics* 923 (2021).

[39] D.I. Pullin. “The large-scale structure of unsteady self-similar rolled-up vortex sheets”. In: *Journal of Fluid Mechanics* 88.3 (1978), pp. 401–430.

[40] D.I. Pullin and W.R.C. Phillips. “On a generalization of Kaden’s problem”. In: *Journal of Fluid Mechanics* 104 (1981), pp. 45–53.

[41] M. Rabaud and Y. Couder. “A shear-flow instability in a circular geometry”. In: *J. Fluid Mech.* 136 (1983), pp. 291–319.

[42] P.G. Saffman. *Vortex Dynamics*. Cambridge University Press, 1992.

[43] S.-I. Sohn. “Numerical simulations of circular vortex sheets by using two regularization models”. In: *J. Korean Phys. Soc.* 63 (2013), pp. 1583–1590.

[44] K. Stewartson. “On almost rigid rotations”. In: *J. Fluid Mech.* 3 (1957), pp. 17–26.

[45] Hui Sun, David Uminsky, and Andrea L Bertozzi. “A generalized Birkhoff–Rott equation for two-dimensional active scalar problems”. In: *SIAM Journal on Applied Mathematics* 72.1 (2012), pp. 382–404.

[46] Sijue Wu. “Recent Progress in Mathematical Analysis of Vortex Sheets”. In: *Proceedings of the ICM* 3 (2003), pp. 233–242.

[47] Sijue Wu. “Mathematical analysis of vortex sheets”. In: *Communications on Pure and Applied Mathematics: A Journal Issued by the Courant Institute of Mathematical Sciences* 59.8 (2006), pp. 1065–1206.